LA-UR-18-23227 (Accepted Manuscript)

Finite-Element Simulations of Elastoplastic Flow during Compression of a Sample in a Diamond Anvil Cell under Extremely High Pressure: Effects of Geometry and Material Properties

Feng, Biao
Levitas, Valery

To be published in: Physical Review Applied

DOI to publisher's version: 10.1103/PhysRevApplied.10.064060

Permalink to record: http://permalink.lanl.gov/object/view?what=info:lanl-repo/lareport/LA-UR-18-23227

Finite element simulations of compression of a sample in diamond anvil cells under extreme high pressures: Effects of geometry and material properties

Biao Feng[1] and Valery I. Levitas[2,*]

[1]*Los Alamos National Laboratory, Los Alamos, NM 87545, United States*

[2]*Departments of Aerospace Engineering, Mechanical Engineering, and Material Science and Engineering, Iowa State University, Ames, IA 50011, United States*

Abstract In this paper, finite element simulations are conducted to investigate large elastoplastic deformations of rhenium under multi-megabar pressures in diamond anvil cells (DAC), with an emphasis on the effects of geometric and material properties. When a small flat cullet surface is used at the center of a diamond, the known experimental pressure distribution and double cupping phenomenon at a pressure of 300 GPa are reproduced. It is found that the material plastic flow initially from the center to the periphery changes to the partial flow to the center, and then changes to elastic deformation at the center under an increasing force. This is caused by double cupping of the diamond under extreme pressures. The paradoxical result that material flow to the sample center does not change the sign of the contact shear stress and pressure gradient is explained by finding that, due to deformation of the diamond, relative contact sliding between the diamond and sample does not change the sign or is absent. Under the same applied load, an increase in the cullet radius reduces pressure and increases thickness of the sample under the cullet, but does not affect them at the beveled surface until cupping appears. However, for the same maximum pressure, an increase in the cullet radius increases pressure everywhere (except for the

* Corresponding author.
Email address for Valery Levitas: vlevitas@iastate.edu
Email address for Biao Feng: fengbiao11@gmail.com

very center), total force, and bending of an anvil both at the center and periphery. An increase in the bevel angle increases pressure gradient and pressure at the center and cupping at the center, but reduces cupping at the periphery, at the same applied force. An increase in sample thickness reduces pressure gradient and pressure at the initial compression stages. This effect reduces and disappears at large compression. Small weaker sample within gasket slightly reduces pressure in a sample but does not affect gasket. The obtained results help to understand the material mechanical response under extreme pressures and large elastoplastic deformations and are beneficial for the optimum design of DAC with the goal of reaching the high and record high pressure single or multiple times.

Keywords: High pressure, Diamond anvil cells, Plasticity, Finite element method, Geometric properties, Yield strength

I. INTRODUCTION

By compressing a sample between two diamond anvils in a diamond anvil cell (DAC), static megabar pressures are generated in experiments [1-5]. In order to find new physical phenomena and new materials, the pressure level need to be increased and meanwhile anvils should not break during single or multiple experimental runs. As an important example, we refer to the recent discussion in *Science* [6-8]: Metallic hydrogen was obtained in [6] under pressure of 495 GPa. It was stated in the critical comment [7] that they had 96% failed diamonds while attempting to reach 350 GPa and criticized about, in particularly, the method of estimation of pressure based on the applied force used in [6]. It was written in the response [8], achievable pressure strongly depends on the geometry of an anvil, thickness of a gasket, and the degree of cupping of the diamond (i.e., appearance of a cup-like concave shape of the contact diamond-sample surface). Very detailed experimental study of the pressure distribution and deformation of an anvil and sample in the megabar pressure range was presented in [3] and [9].

Numerical modeling of compression of a sample in DAC is related to significant theoretical and computational problems due to multiple physical, geometric, and contact nonlinearities. Geometric nonlinearity is related to large elastic and plastic deformations, material rotations, and displacements. Physical nonlinearities are caused by nonlinear elasticity rules, plasticity of a sample, and pressure-dependence of the yield strength. Contact nonlinearities are due to contact relative sliding with unknown sliding and cohesion zones, and the deformed surfaces.

Finite element method (FEM) is widely used to study the stress-strain states of sample and anvils in DAC [10-17]. Moss *et al*. found by FEM that the increase in the yield strength of a gasket plays the key role in achieving extreme high pressure [10]. By using the “Supreme 63” tool metal

with the yield strength of 2.5 GPa as the gasket material they claimed to achieve the pressures of 460 GPa experimentally. Moss and Goettel performed finite element analyses of beveled diamond anvils and discussed the design of a diamond anvil by changing culet geometries [11]. Merkel *et al*. [13] extended previous FEM calculations [10, 11] to simulate the experiment on compression of a rhenium sample up to 300 GPa [3], and to numerically study effects of geometric parameters of the sample and anvil system [15]. Coupled plastic flows and strain-induced phase transforms in the sample in DAC [18-20] and rotational DAC (RDAC) [21-23] were investigated, with assumptions of the sample with small elastic and transformational strains and the diamond anvils as rigid body.

Previous models [10-13, 15] were not based on a fully large-strain framework and therefore are unable to reproduce some experimental phenomena (e.g., pressure distribution) under the extreme condition of several megabar pressures. In most of these works, equations were not given and results of simulations using some available FEM codes were presented. Recently, Feng *et al*. [14, 24] formulated a thermodynamically consistent system of equations considering large elastic and plastic deformation of a sample and large elastic deformation of the diamond anvil, and successfully reproduced with FEM the experimental pressure distribution [3] at a pressure up to 300 GPa. They also revealed numerically a pressure self-focusing effect [16, 24], which allows one to achieve extremely large pressure gradient and consequently high pressure at the center of a sample. These studies were extended on a 3D problem on compression and torsion of a sample in RDAC under extreme pressures [16, 24].

It is well known that the geometric and material properties are essential to determine the material responses under the extreme high pressure. The use of *beveled* diamond anvils in DAC is the key to generate static pressures above 1 Megabar [5, 25]. However, the choice of the bevel

angle experimentally is expensive because of fracture of one or both anvils [11]. That is the reason why the FEM simulations are important for optimization of the geometry. In addition, since the introduction of gasket into a DAC is a milestone in the history of DAC [25], the study of the system of gasket and sample under megabar pressures by using FEM is very important but was not done in previous work.

In this paper, we study the effects of geometric and material properties in DAC, based on the advanced large deformation framework developed in [14, 24]. A total system of equation is presented in Section II. Stresses and plastic flow for the culler radius $R = 5\,\mu\text{m}$, bevel angle $\alpha = 8.5^{o}$ and initial sample thickness $h_0 = 20\,\mu\text{m}$ were studied in Section III.B. In particular, experimental pressure distribution [3], double cupping [26], and cupping-related pressure drop [3, 26] were reproduced numerically. Transition from plastic flow from the center, to partial flow to the center, and then to elastic deformation, all under increased loading, is reproduced. Deformation of the diamond anvil plays a crucial role in this phenomenon. It also explains why when velocity changes the sign friction stress and pressure gradient does not: because relative sliding velocity with respect to diamond is either zero or positive. Effect of the radius of the flat surface is studied in Section III.C. Results are quite different for the same applied load or the same maximum pressure. Effect of the bevel angle is analyzed in Section III.D. Increase in the bevel angle increases the pressure gradient and pressure at the center and cupping at the center, but reduces cupping at the periphery. It is shown in Section III.E that the increase in sample thickness reduces the pressure gradient and pressure at the initial compression stage. This effect reduces and disappears at large compression. In Section III.F we demonstrate that in a small sample that has two time smaller yield strength at zero pressure than gasket, reduction in pressure is relatively small and change in pressure distribution in gasket is negligible. Section IV contains concluding remarks.

Specifically, we study the effect of a cullet radius (the flat part at the center of sample and diamond contact surface), and reveal the material mechanical response with an increasing loading. By using the third-order elastic constants from [27], the cupping at the pressure of 300 GPa in

experiments [3] was not reproduced in our previous simulations [14]. Thus, we adjusted the third-order elastic constants in [14] to reproduce cupping. We find here that this is caused by the absence of the flat part of the diamond in the previous simulations [14]. With the flat cullet, we reproduced both pressure distribution and cupping using the third-order elastic constants from [27]. Also, we obtained double cupping (i.e., concave parts at the center and periphery of an anvil), which was observed in recent experiments [26]. Second, the effects of the radius of the flat cullet, the bevel angle, and initial thickness of a sample is studied and discussed in detail. Third, the sample and gasket system is treated for the first time for extreme pressures to study the effects of sample strength. The obtained results help to understand the material mechanical responses under extreme conditions of high pressures and plastic deformations, and are beneficial for the optimum designs of a DAC system.

II. PROBLEM FORMULATION

II.A. Geometry and boundary conditions

A schematic of a DAC is shown in the Fig. 1a, where a normal stress σ_n is applied on the diamond surface and a sample is compressed by two diamond anvils. We ignore the anisotropy of diamond anvil in the circumferential direction to use an axisymmetric formulation. Because of axisymmetric loads and geometry of DAC and the symmetry with respect to the horizontal plane *IJ* in Fig. 1c, we consider a quarter of DAC as shown in Fig. 1b. The major geometric parameters for an anvil and for contact surface between diamond and sample are given in Fig. 1b and 1c, respectively. The geometry of the preindented sample is shown in Fig. 1c along with the zoomed central part. A half of sample thickness at the r=0 in the initial undeformed configuration is $h_0/2$ (line *CI* in Fig. 1c). The undeformed shape of contact surface is as follow: from point *C* at the r=0

to point *R*, there is a small flat region with the radius r_0; from point *R* to point *G*, the contact surface is inclined with initial bevel angle α; at the periphery line *GE* has a inclined angle 43.27°; the radial distance between *CG* is 150 μm; the radial distance *IJ* at the symmetry plane is 772.5 μm, which is long enough to exclude the boundary effect of the right end *HJ*; the thickness of the boundary *HJ* is 125 μm. We will discuss the effects of geometric parameters by varying h_0, r_0, and α.

The boundary conditions for a quarter of DAC in Fig. 2b are listed as follows:

(1) The normal stress σ_n is applied at the top surface *AB* of the DAC (as also shown in Fig. 1a).

(2) At the *z* axis (the symmetry axis $r = 0$) (line *AC* for the anvil in Fig. 1b and line *CI* for the sample in Fig. 1c), shear stress τ_{rz} and the radial displacement u_r are zero.

(3) At the contact surface (*CRGE* shown in Fig. 1c), the Coulomb friction model is applied. When friction stress reaches $\mu\sigma_c$, slipping is allowed (σ_c is the normal contact stress at the contact surface between the diamond and the sample, and μ is the Coulomb friction coefficient). Otherwise, the cohesion condition, i.e., continuity of displacements, is applied.

(4) At the symmetry plane $z = 0$ (plane *IJ* in Fig. 1c), the radial shear stress $\tau_{rz} = 0$, and the axial displacement $u_z = 0$.

(5) Other surfaces not mentioned above are stress-free.

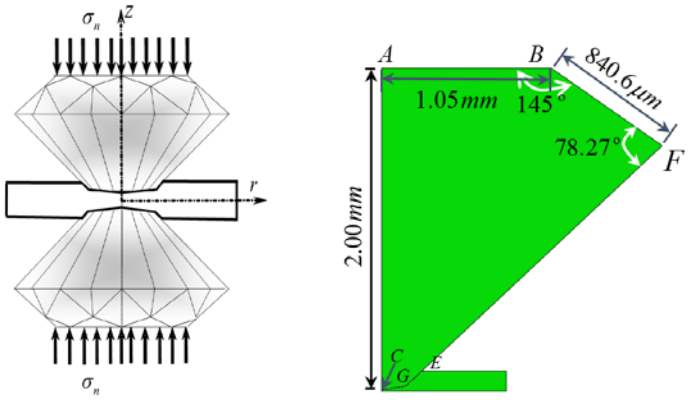

(a) (b)

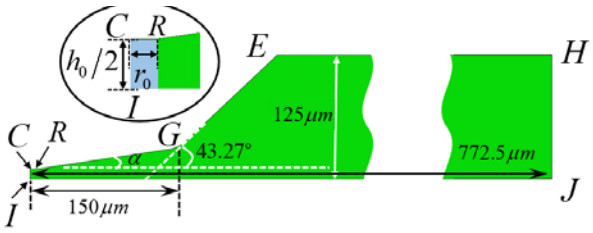

(c)

FIG. 1. Geometric parameters of diamond anvil cell and sample. (a) Diamond anvil cell scheme, (b) a quarter of the sample and anvil in the initial undeformed state and the geometry of anvil, and (c) the geometry of a sample and a zoomed-in center part of a sample, which is placed in the ellipse.

II.B. A complete system of equations for large-strain elastoplasticity for a sample

In this paper, the complete system of equations for both sample and diamond anvil are summarized from [14] and [16], and computational algorithms proposed in [14] are used for the current models.

Contractions of the second-order tensors $\boldsymbol{A} = \{A_{ij}\}$ and $\boldsymbol{B} = \{B_{ij}\}$ over one and two indices are designated as $\boldsymbol{A} \cdot \boldsymbol{B} = \{A_{ij} B_{jk}\}$ and $\boldsymbol{A} : \boldsymbol{B} = \{A_{ij} B_{ji}\}$, respectively. The subscripts *s* and *a* designate symmetrization and anti-symmetrization, respectively, the subscripts *e* and *p* represent elastic and plastic deformation gradient or strain, the superscripts -1 and *t* means the inverse and transposition of a tensor, and $\boldsymbol{I}$ is the second-order unit tensor.

Kinematics. The motion of material with large elastic and plastic deformations is described by a vector function $\boldsymbol{r} = \boldsymbol{r}(\boldsymbol{r}_0, t)$, where $\boldsymbol{r}$ and $\boldsymbol{r}_0$ are the position vectors of material points in the actual configuration Ω at time instant t and in the reference configuration Ω_0 at the instant t_0, respectively. The deformation gradient

$$\boldsymbol{F} = \frac{\partial \boldsymbol{r}}{\partial \boldsymbol{r}_0} = \boldsymbol{F}_e \cdot \boldsymbol{F}_p = \boldsymbol{R}_e \cdot \boldsymbol{U}_e \cdot \boldsymbol{R}_p \cdot \boldsymbol{U}_p = \boldsymbol{R}_e \cdot \boldsymbol{U}_e \cdot \boldsymbol{U}_p = \boldsymbol{V}_e \cdot \boldsymbol{R}_e \cdot \boldsymbol{U}_p, \ \left(\boldsymbol{R}_p = \boldsymbol{I};\ \boldsymbol{V}_e = \boldsymbol{R}_e \cdot \boldsymbol{U}_e \cdot \boldsymbol{R}_e^T\right) \quad (1)$$

is decomposed into elastic $\boldsymbol{F}_e$ and plastic $\boldsymbol{F}_p$ contributions, where $\boldsymbol{F}_p$ is the deformation gradient obtained after a complete release of stresses in the local vicinity of each material point, $\boldsymbol{U}_p$ and

$\boldsymbol{U}_e$ are the symmetric plastic and elastic right stretch tensors, $\boldsymbol{R}_e$ and $\boldsymbol{R}_p$ are the proper orthogonal elastic and plastic rotation tensors, and $\boldsymbol{V}_e$ is the elastic left stretch tensor.

Lagrangian and Eulerian elastic strain tensors are

$$\boldsymbol{E}_e = 0.5\left(\boldsymbol{U}_e \cdot \boldsymbol{U}_e - \boldsymbol{I}\right); \qquad \boldsymbol{B}_e = 0.5\left(\boldsymbol{V}_e \cdot \boldsymbol{V}_e - \boldsymbol{I}\right). \tag{2}$$

Decomposition of the velocity gradient $\boldsymbol{l} = \dot{\boldsymbol{F}} \cdot \boldsymbol{F}^{-1} = \boldsymbol{W} + \boldsymbol{d}$ into antisymmetric spin tensor $\boldsymbol{W} = \left(\boldsymbol{l}\right)_a$ and symmetric deformation rate $\boldsymbol{d} = \left(\boldsymbol{l}\right)_s$ are accepted. In combination with Eq. (1), we obtain the following decomposition of the deformation rate $\boldsymbol{d}$ into elastic and plastic contributions:

$$\boldsymbol{d} = \overset{\nabla}{\boldsymbol{B}}_e - 2\left(\boldsymbol{d} \cdot \boldsymbol{B}_e\right)_s + \boldsymbol{V}_e \cdot \boldsymbol{D}_p \cdot \boldsymbol{V}_e; \quad \boldsymbol{D}_p = \boldsymbol{R}_e \cdot (\dot{\boldsymbol{U}}_p \cdot \boldsymbol{U}_p^{-1})_s \cdot \boldsymbol{R}_e^t; \quad \overset{\nabla}{\boldsymbol{B}}_e = \dot{\boldsymbol{B}}_e - 2\left(\boldsymbol{W} \cdot \boldsymbol{B}_e\right)_s, \tag{3}$$

where $\overset{\nabla}{\boldsymbol{B}}_e$ is the Jaumann objective time derivative and $\boldsymbol{D}_p$ is the plastic deformation rate.

Elasticity rule. The following isotropic nonlinear elastic rule will be used

$$\boldsymbol{\sigma} = \frac{1}{det\boldsymbol{F}}(2\boldsymbol{B}_e + \boldsymbol{I}) \cdot \frac{\partial \Psi}{\partial \boldsymbol{B}_e}, \tag{4}$$

where $det\boldsymbol{F}$ is the determinant of the tensor $\boldsymbol{F}$, $\boldsymbol{\sigma}$ is Cauchy stress, and the most popular elastic potential Ψ for the extreme condition of high pressure is the third-order Murnaghan potential [28]:

$$\Psi\left(\boldsymbol{B}_e\right) = \frac{\lambda_e + 2G}{2} I_1^2 - 2GI_2 + \left(\frac{l + 2m}{3} I_1^3 - 2mI_1 I_2 + nI_3\right), \tag{5}$$

where λ_e, G, l, m, and n are elastic material parameters and I_1, I_2, and I_3, are the first, second and third invariants of the strain tensor $\boldsymbol{B}_e$:

$$I_1 = B_{e_{11}} + B_{e_{22}} + B_{e_{33}}; \quad I_2 = B_{e_{22}} B_{e_{33}} - B_{e_{23}}^2 + B_{e_{11}} B_{e_{33}} - B_{e_{13}}^2 + B_{e_{22}} B_{e_{11}} - B_{e_{12}}^2; \quad I_3 = det\,\boldsymbol{B}_e. \tag{6}$$

Plasticity. The pressure-dependent J_2 flow theory is used with the yield surface

$$\varphi = \sqrt{3/2\boldsymbol{s} : \boldsymbol{s}} - \sigma_y\left(p, q\right) = 0, \tag{7}$$

where $\boldsymbol{s}$ is the deviatoric Cauchy stress, $\boldsymbol{\sigma}_y$ is the yield strength, which depends on the mean pressure p and accumulated plastic q defined as

$$\dot{q} = \left(2\,\boldsymbol{D}_p : \boldsymbol{D}_p / 3\right)^{0.5}. \tag{8}$$

The plastic flow rule is presented as

$$\boldsymbol{D}_p = \lambda \, \boldsymbol{s} \Big/ \sqrt{\boldsymbol{s} : \boldsymbol{s}}, \tag{9}$$

where λ $(\lambda > 0)$ is a scalar function determined from the consistency condition $\dot{\varphi} = 0$.

The traditional equilibrium equations in the current configuration are used

$$\nabla \cdot \boldsymbol{\sigma} = \boldsymbol{0}. \tag{10}$$

It was found in [29] for more than 60 materials belonging to different classes (*e.g.*, metals, rocks, alloys, oxides, compacted powders), above some level of plastic strain and for a deformation path without sharp changes in directions (monotonous deformation), the initially-isotropic polycrystalline materials are deformed as a perfectly plastic and isotropic material with a strain history-independent limiting surface of the perfect plasticity. It excludes accumulated plastic strain *q* from the relationship for the yield strength in Eq. (7), $\sigma_y(p,q) = \sigma_y(p)$. The linear dependence of yield strength on pressure *p* is accepted in this paper

$$\sigma_y(p) = \sigma_{y0} + bp, \tag{11}$$

where σ_{y0} is the yield strength at the pressure *p*=0 and *b* is a parameter.

Material parameters. Rhenium has been of particular interest because of its large bulk (*K*) and shear (*G*) moduli and high strength [4, 30] and it is widely used as the sample and gasket material in a DAC [1-4]. The following properties of rhenium are used in simulations: Elastic constants [4, 14, 30] $G = 200$ GPa , $\lambda_e = 247$ GPa , $l = -291$ GPa , $m = -662$ GPa and n=0, and plastic constants [4, 14] $\sigma_{y0} = 8.00$ GPa and $b = 0.04$.

II.C. Nonlinear anisotropic elasticity for single-crystal diamond

The traditional elasticity rule has the form

$$\boldsymbol{\sigma} = \boldsymbol{F}\cdot\tilde{\boldsymbol{T}}\left(\boldsymbol{E}\right)\cdot\boldsymbol{F}^{t}\big/det\boldsymbol{F}; \qquad \boldsymbol{T} = \boldsymbol{\sigma} det\boldsymbol{F} = \boldsymbol{F}\cdot\tilde{\boldsymbol{T}}\left(\boldsymbol{E}\right)\cdot\boldsymbol{F}^{t}; \qquad \tilde{\boldsymbol{T}} = {}^{\partial\Psi}\big/_{\partial\boldsymbol{E}}, \tag{12}$$

where $\boldsymbol{T}$ is the Kirchhoff stress, $\tilde{\boldsymbol{T}}$ is the second Piola-Kirchhoff stress, and since there is no plastic deformation in a diamond, the subscript *e* is dropped. Under megabar pressures, it is necessary to consider at least the third-order potential Ψ with the cubic symmetry:

$$\begin{aligned}\Psi &= 0.5c_{11}\left(\eta_1^2+\eta_2^2+\eta_3^2\right)+c_{12}\left(\eta_1\eta_2+\eta_1\eta_3+\eta_2\eta_3\right)+0.5c_{44}\left(\eta_4^2+\eta_5^2+\eta_6^2\right)+c_{111}\left(\eta_1^3+\eta_2^3+\eta_3^3\right)/6\\ &+0.5c_{112}\left[\eta_1^2\left(\eta_2+\eta_3\right)+\eta_2^2\left(\eta_1+\eta_3\right)+\eta_3^2\left(\eta_1+\eta_2\right)\right]+c_{123}\eta_1\eta_2\eta_3+0.5c_{144}\left(\eta_1\eta_4^2+\eta_2\eta_5^2+\eta_3\eta_6^2\right)\\ &+0.5c_{166}\left[\left(\eta_2+\eta_3\right)\eta_4^2+\left(\eta_1+\eta_3\right)\eta_5^2+\left(\eta_1+\eta_2\right)\eta_6^2\right]+c_{456}\eta_4\eta_5\eta_6,\end{aligned} \tag{13}$$

where $\eta_1 = E_{11}$, $\eta_2 = E_{22}$, $\eta_3 = E_{33}$, $\eta_4 = 2E_{23}$, $\eta_5 = 2E_{31}$, and $\eta_6 = 2E_{12}$.

In this paper, the second-order elastic constants are [31]: $c_{11} = 1050\,\text{GPa}$, $c_{12} = 127\,\text{GPa}$, and $c_{44} = 550\,\text{GPa}$ and the third-order elastic constants are [27]: $c_{111} = -7603\text{GPa}$, $c_{112} = -1909\text{GPa}$, $c_{123} = -835\text{GPa}$, $c_{166} = -3938\text{GPa}$, $c_{144} = 1438\text{GPa}$, and $c_{456} = -2316\text{GPa}$.

In simulations, the friction coefficient in the Coulomb friction rule is $\mu = 0.1$.

III. RESULTS AND DISCUSSION IN THE SAMPLE UNDER EXTREME PRESSURES

III.A. Overview

Our results [14] reproduced the pressure distribution in experiments [3] up to 300 GPa. The cupping was observed experimentally [3] under the pressure around 300 GPa but it does not appear in our simulations [14] when we used the third order elastic constants from [27]. The reason will be found out that a very short flat contact surface (the line *CR* in Fig. 1c) is used in experiments but it was ignored in the previous FEM simulations [14]. At the beginning of this section, we will use the flat part $r_0 = 5\,\mu\text{m}$ and the beveled angle $\alpha = 8.5^{\circ}$, which are taken from experiments [3]. The sample is assumed to be pre-indented into the initial thickness as $h_0 = 20\,\mu\text{m}$ at the center

(r=0), which is commonly used in experiments (see [1]). This set of geometric parameters ($r_0 = 5\,\mu\text{m}$, $\alpha = 8.5^o$ and $h_0 = 20\,\mu\text{m}$) are used for results in Figs. 2-4. To study the effects of the radius of the flat part r_0 in Figs. 5 and 6, we vary r_0 from 0 to 5 and 10 μm, with the fixed $\alpha = 8.5^o$, and $h_0 = 20\,\mu\text{m}$. The effects of beveled angle in Fig. 7 is studied by comparing the results with $\alpha = 7.5^o$ and 9.5^o for $r_0 = 10\,\mu\text{m}$ and $h_0 = 20\,\mu\text{m}$. Fig. 8 shows the effects of initial thickness of sample by comparing results for $h_0 = 20$ and 40 μm, with $\alpha = 8.5^o$ and $r_0 = 0\,\mu\text{m}$. The effect of the sample strength will be studied by comparing the results of $\sigma_{y0} = 8.00\,\text{GPa}$ and $\sigma_{y0} = 4.00\,\text{GPa}$, with the same gasket properties and the geometrical parameters: $h_0 = 10\,\mu\text{m}$ with $\alpha = 9.5^o$ and $r_0 = 10\,\mu\text{m}$.

III.B. Stresses and plastic flow for $r_0 = 5\,\mu\text{m}$, $\alpha = 8.5^o$ and $h_0 = 20\,\mu\text{m}$

Fig. 2 plots the distributions of pressure and shear stress under an increasing applied stress σ_n. Our simulation results in curve 4 coincide with experimental data in [3]. The major difference between the current and previous simulation results [15] is that the pressure gradient in this paper is much larger at the center of sample but smaller at the periphery than that in [15].

Distribution of shear stresses (friction stress) τ_f in Fig. 2b coincides with the distribution of the pressure-dependent yield strength in shear $\tau_y(p)$ for most of contact region with a low load (see curve 1 and 2). This means that plastic friction condition $\tau_f = \tau_y(p)$ is fulfilled in this region. While it is not included explicitly in the contact sliding condition, it means that localized plastic flow in a thin contact layer occurs, which is equivalent to the contact sliding. With an increase of compressive loads from curve 3 to curve 5, the shear stress decreases at the center of sample, and

there is an increasing region where the friction stress τ_f is smaller than $\tau_y(p)$. This is caused by changing the direction of material flow as shown in Fig. 3.

In [14], even without the flat part *CR* ($r_0 = 0$), the pressure distribution was also consistent with experiments, but the cupping at the pressure around 300GPa was not reproduced. With a short flat part, case 5 in Fig. 3 clearly showed that the cupping appears at σ_n=3.011 GPa, where the maximum pressure is 300 GPa at the center in Fig. 2a. Here we should mention that cupping can cause the sudden drop of pressure distribution at periphery as it is seen in curve 5 at $r = 140$ μm. Similar pressure drop due to cupping can be found in this paper for all other cases with different geometric parameters. What is more important that similar cupping-related pressure drop was observed in experiments [26].

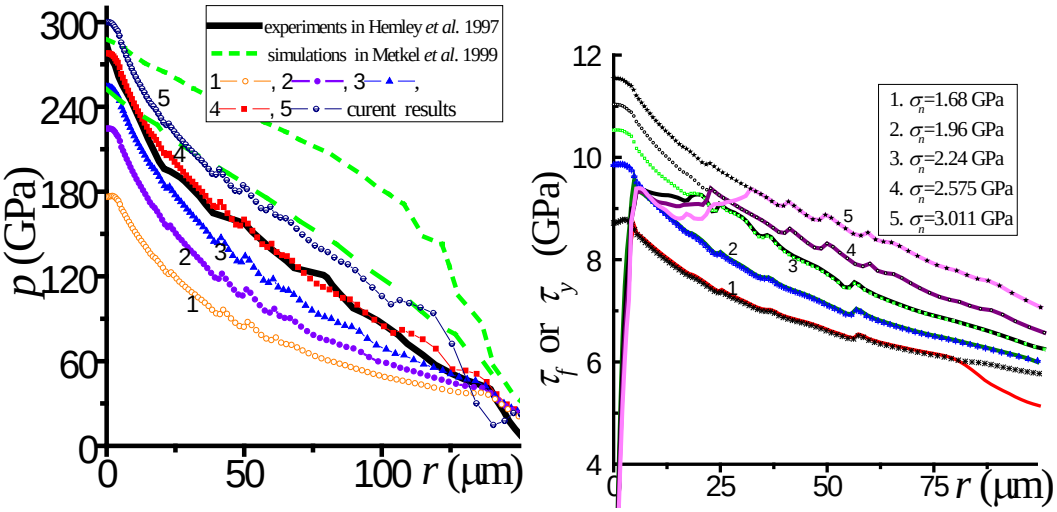

(a) (b)

Fig. 2. Distributions of pressure *p* (a) and friction stress τ_f (solid lines) and yield strength in shear τ_y (doted lines) (b) at the contact surface of a sample for $r_0 = 5$μm under an increasing applied normal stress σ_n: 1.68 GPa (1), 1.96 GPa (2), 2.24 GPa (3), 2.575 GPa (4), and 3.011 GPa (5). In (a) doted curves 1-5 are the current simulation results, two green dashed

curves are the simulations results from Ref. 9, and the solid black curve is the experimental results in Ref. 3.

Important information can be learned from Figs. 3 and 4, which present the velocity along the radial direction v_r and the rate of accumulated plastic strain $\dot{q}$. Since for the current rate-independent plasticity and static problem formulation time is not parameter, the magnitudes of $\dot{q}$ and v_r can be made arbitrary by changing the rate of loading. This does not change stress and strain distribution at each load, independent how fast it is achieved. Results in Figs. 3 and 4 are presented for constant $\dot{\sigma}_n = 0.7 \times 10^{-4}\,\text{GPa/s}$. Consequently, only relative values in distributions of $\dot{q}$ and v_r for any state (or load σ_n) are important. It is found from Fig. 3 that initially at $\sigma_n = 1.68\,\text{GPa}$ the whole sample flows "fast" from the center to the periphery. With an increase in applied force σ_n, starting from the center of sample, the radial velocity v_r changes the direction and materials "slowly" moves from the periphery to the center. For $\sigma_n = 3.011\,\text{GPa}$, material motion towards the center is observed in the major region of a sample.

It looks very counterintuitive that material velocity changes sign within a sample but contact shear stresses in Fig. 2b do not. The negative velocity v_r and its gradient along the thickness direction are very small (by one order of magnitude) in comparison with material flows from the center to the periphery at the external part of a sample. Since plastic flow is incompressible, deformation in this region is either elastic or with small plastic strains. This is in agreement with small values of $\dot{q}$ in this region (Fig. 4). The key point is that due to deformation of diamond, relative sliding velocity at the contact surface is either zero or positive, that is why contact shear stress does not change sign.

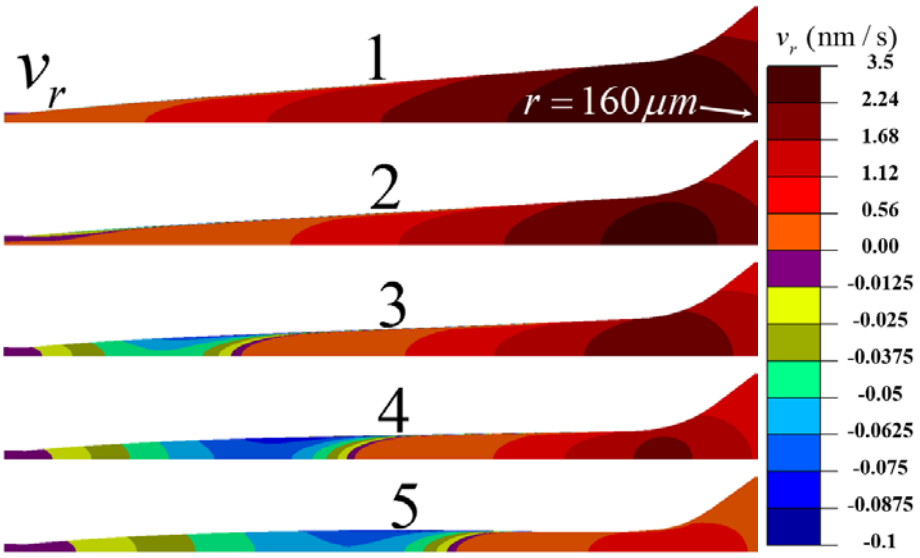

Fig. 3. Distribution of radial velocity v_r in the sample $(0 \le r \le 160\,\mu m)$ with $r_0 = 5\,\mu m$ under an increasing applied normal stress σ_n. The normal stress σ_n is 1.68 GPa (1), 1.96 GPa (2), 2.24 GPa (3), 2.575 GPa (4), and 3.011 GPa (5).

Fig. 4 shows the distribution of the rate of accumulated plastic strain $\dot{q}$. Initially at σ_n =1.68 GPa, the entire region is under plastic straining. The accumulated plastic strain rate shows the shear band near the contact surface, where shear stresses reached the yield strength in shear. Excluding this region, $\dot{q}$ is not very heterogeneous along the radius. This is because the radial velocity increases with *r* but the sample thickness increases as well. As the applied stress σ_n increases from 1.96 GPa to 2.24 GPa, in the region with negative velocity v_r in Fig. 3 $\dot{q}$ is nonzero but quite small. With the further increase of applied stresses, the rate of accumulated plastic strain significantly reduces and the location with the maximum accumulated plastic rate moves towards the periphery. At σ_n =2.575 GPa, $\dot{q}$ becomes zero at the center of a sample, demonstrating unusual transition from plastic to the elastic state under increased load. The region without plastic deformation grows and $\dot{q}$ decreases in the rest of the sample as the σ_n increases. One of the reason for this is that the

bending of anvil slows down thickness reduction rate. As a result, the pressure and pressure gradient cannot continuously increase when cupping becomes significant (see also experiment in Ref. 3), which can be explained by a simplified equilibrium equation (see, e.g. [16, 29, 32])

$$\frac{dp}{dr} = -\frac{2\tau_f}{h}. \tag{14}$$

Indeed, the thickness h cannot further be reduced after some critical value.

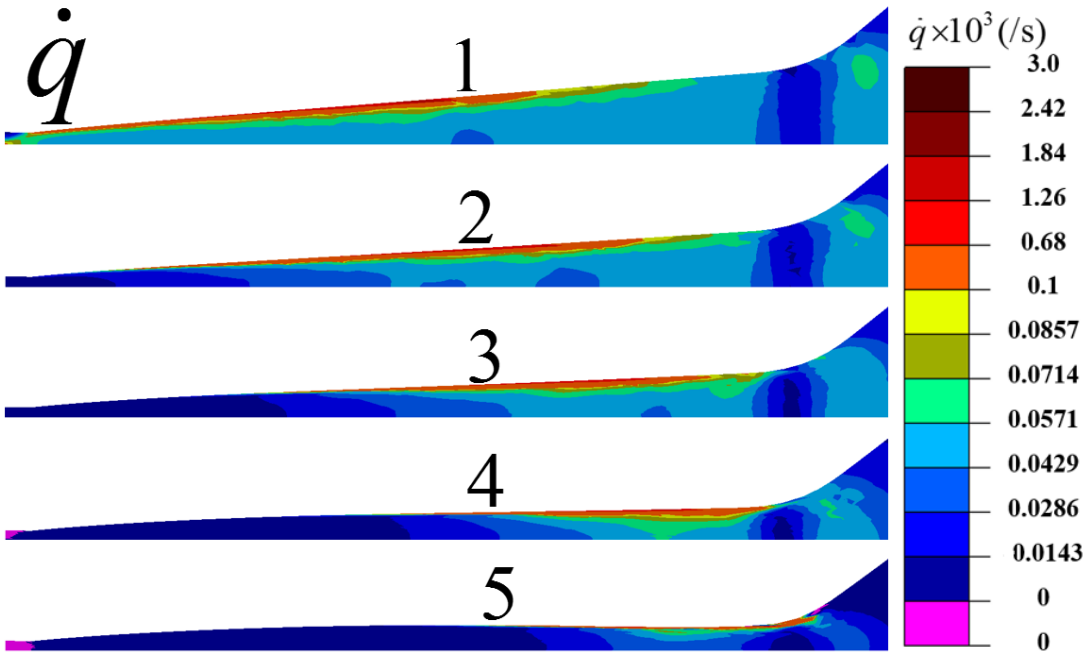

Fig. 4. Distributions of the rate of accumulated plastic strain $\dot{q}$ in the sample $(0 \le r \le 160\,\mu\text{m})$ with $r_0 = 5\,\mu\text{m}$ under an increasing applied normal stress σ_n. The normal stress σ_n is 1.68 GPa (1), 1.96 GPa (2), 2.24 GPa (3), 2.575 GPa (4), and 3.011 GPa (5). In the magenta region plastic strain rate is exactly zero.

III.C. Effect of the radius of the flat cullet

Fig. 5 plots the distributions of pressure and the *z* coordinate of the contact surface for radii of the flat cullet r_0 that varies from 0 to 5 to 10 μm , when *the maximum pressure reaches 293 GPa*. A

shorter flat part *CR* means the a longer inclined part *RG* in Fig. 1c, since the radial distance *CG* is fixed at 150 μm. At a given applied stress σ_n but with different r_0, the shorter the cullet radius r_0 is, the faster the plastic flow along the radial direction and the thickness reduction are because the inclined diamond surface with positive slope instead of the flat cullet favors the material flows to the periphery. The faster thickness reduction causing a larger pressure and pressure gradient at the center due to simplified equilibrium condition (14). It indicates that for the same maximum pressure at the center, the applied normal stress σ_n is an increasing function of the radius of the flat part r_0 (Fig. 5). Fig. 5b plots the *z* coordinate of the contact surface (equal to half a thickness of sample $h/2$) for r_0 = 0, 5 and 10 μm. The smaller r_0 and consequently σ_n leads to a faster thickness reduction at the center, but smaller deformation of an anvil both at the center and at periphery. Cupping near the sample center appears for any initially flat surface; it increases with increasing r_0. At the periphery, the cupping does not appear with r_0 =0; it just appears for r_0 =5, and becomes very obvious for 10 μm. Similar to Fig. 2a the cupping causes the pressure drop at the periphery for r_0 =10 μm in Fig. 5a, like in experiment [26]. Thus, for *the same maximum pressure*, an increase in the cullet radius essentially increases pressure everywhere except for the center, total force, bending of an anvil both at the center and periphery.

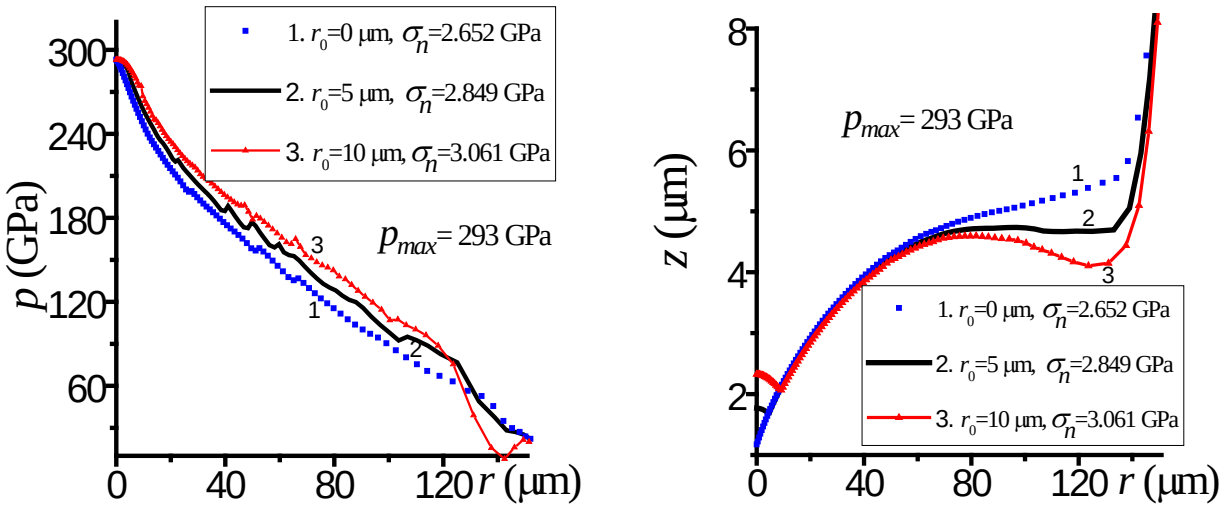

(a) (b)

Fig. 5. Distributions of the pressure p at the sample contact surface (a) and the z coordinate of diamond/sample contact surface (b) when the maximum pressure is p= 293 GPa at r=0 at the contact surface. The applied stress σ_n is 2.652 GPa (1), 2.849 GPa (2), 3.061 GPa (3). PLEASE CHANGE IN FIG d TO R

Very different conclusions can be made if one compares the effect of the cullet radius r_0 at 0 and 10 μm on the distribution of pressure and the profile of contact surface at *the same applied load* (Fig. 6). *Under the same applied load, the pressure distribution and thickness of the sample are the same everywhere except for the center of the sample*. For r_0 =0, material flows much faster at the center than for r_0 =10 μm in Fig. 6b, which causes a larger pressure gradient and pressure at the center of sample. With the increasing applied load σ_n, the difference on pressure at the center for both cases becomes more obvious. At σ_n =1.681 GPa, the difference in pressure is only 6 GPa; at σ_n =3.061 GPa, the difference in pressure becomes 21 GPa. This is because as the thickness reduces, the difference in 1/h increases and pressure gradient linearly depends on 1/h. For example,

the ratios of 1/*h* at *r*=0 between r_0=0 and 10 μm is 1.8 with σ_n=1.681 GPa and 2.03 with σ_n =3.013 GPa.

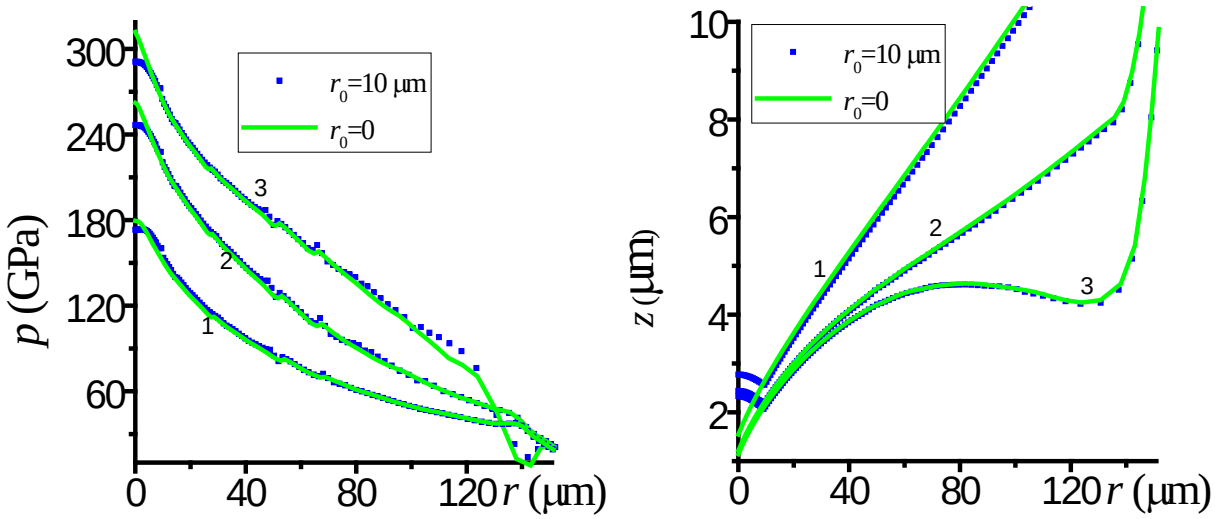

Fig. 6. Distributions of the pressure *p* at the contact surface of a sample and *z* coordinate of the diamond/sample contact surface for $r_0 = 0$ and 10 μm under the applied stress σ_n is 1.681 GPa (1), 2.241 GPa (2) and 3.013 GPa (3).

Comparing curves 2 and 3 in Fig. 6b, one concludes that for maximum pressure above 250 GPa, increase in force does not reduce thickness of a sample for the beveled surface for both $r_0 = 0$ and 10 μm and results in a bending at the periphery of a sample. Cupping at the center does not occur for $r_0 = 0$ and occurs at any force under study for $r_0 = 10$ μm.

III.D. Effect of the bevel angle

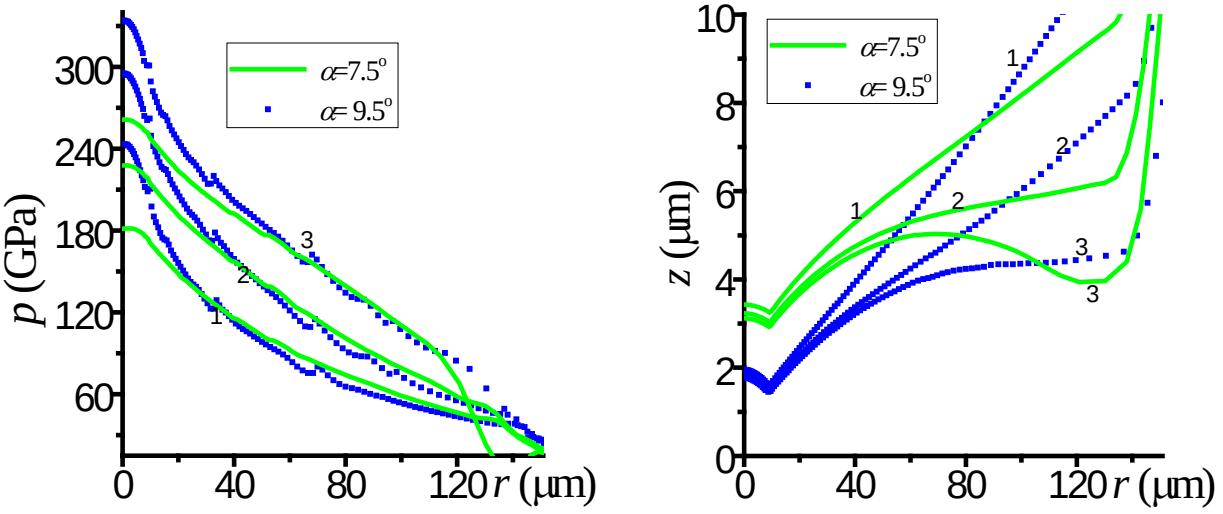

(a) (b)

Fig. 7. Distributions of the pressure p at the contact surface of sample (a) and z coordinate of diamond/sample contact surface (b) for $r_0 = 10$ μm and two bevel angles, $\alpha = 7.5^\circ$ or 9.5°, under three applied normal stress σ_n: 1.868 GPa (1), 2.365 GPa (2), 3.045 GPa (3).

The effect of the bevel angle α is shown in Fig. 7. With a larger beveled angle $\alpha = 9.5^\circ$, the material flow from the center to the periphery is more intense, which causes much faster thickness reduction at the center than for $\alpha = 7.5^\circ$. Smaller thickness of a sample at the center for $\alpha = 9.5^\circ$ causes a larger pressure gradient and pressure at the center than for $\alpha = 7.5^\circ$. In addition, for an larger bevel angle, the cupping at the periphery is postponed: at σ_n=3.045 GPa, the cupping is obvious for $\alpha = 7.5^\circ$ and does not exist for $\alpha = 9.5^\circ$. In addition, cupping at the center is slightly larger for $\alpha = 9.5^\circ$. We note that at the periphery the thickness is smaller for $\alpha = 7.5^\circ$ than for $\alpha = 9.5^\circ$, due to smaller initial thickness and larger diamond bending and cupping. At the periphery, the thickness reduction rate is also faster with a larger bevel angle. For example, the difference of the z coordinate at $r = 120$ μm between cases with $\alpha = 9.5^\circ$ and 7.5° is 1.3 μm, 1.0 μm and 0.5 μm, for the applied load σ_n of 1.4 GPa, 1.75 GPa and 2.652 GPa, respectively.

III.E. Effect of initial sample thickness

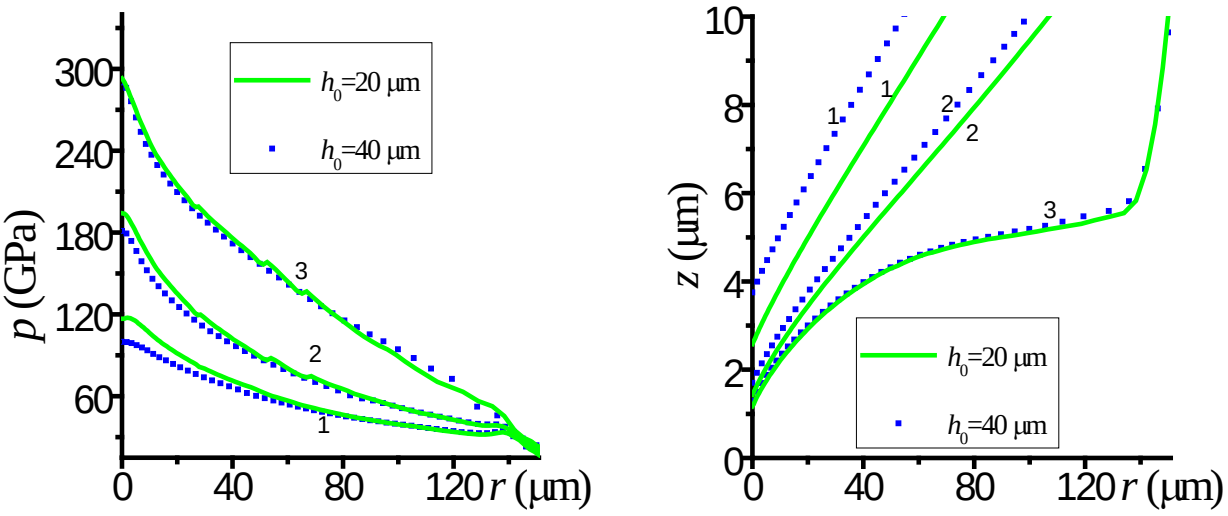

(a) (b)

Fig. 8. Distributions of the pressure *p* at the contact surface of a sample (a) and *z* coordinate of the diamond/sample contact surface (b) for $r_0 = 0\ \mu m$ and initial thicknesses of $h_0 = 20\ \mu m$ or $40\ \mu m$ at the center of sample under the applied normal stress σ_n: 1.4 GPa (1), 1.75 GPa (2), 2.652 GPa (3).

In Figs. 2-7 the sample is pre-indented to the initial thickness of 20 μm at the center. In Fig. 8 we compare results for $h_0 = 20\ \mu m$ with those for $h_0 = 40\ \mu m$. Under a small applied normal stress σ_n =1.4 GPa, Fig. 8b shows material flows to the periphery much faster with a larger initial thickness $h_0 = 40\ \mu m$, because initially the difference of *z* coordinate at the center is 10 μm and it is just 1.2 μm under σ_n =1.4 GPa. Due to a smaller thickness in the deformed configuration, the pressure at the center with the initial thickness with $h_0 = 20\ \mu m$ is 17 GPa larger than the pressure with $h_0 = 40\ \mu m$. With the increase of *r* coordinate, the difference in pressure distribution decreases while difference in *h* practically does not change. It is noted that the differences causing by initial thickness significantly reduces with increase of applied normal stress. At σ_n =2.652 GPa, the distributions of both pressure and the thickness of the sample are almost the same for $h_0 = 20\ \mu m$ and $40\ \mu m$.

III.F. Sample-gasket system: effect of the sample strength

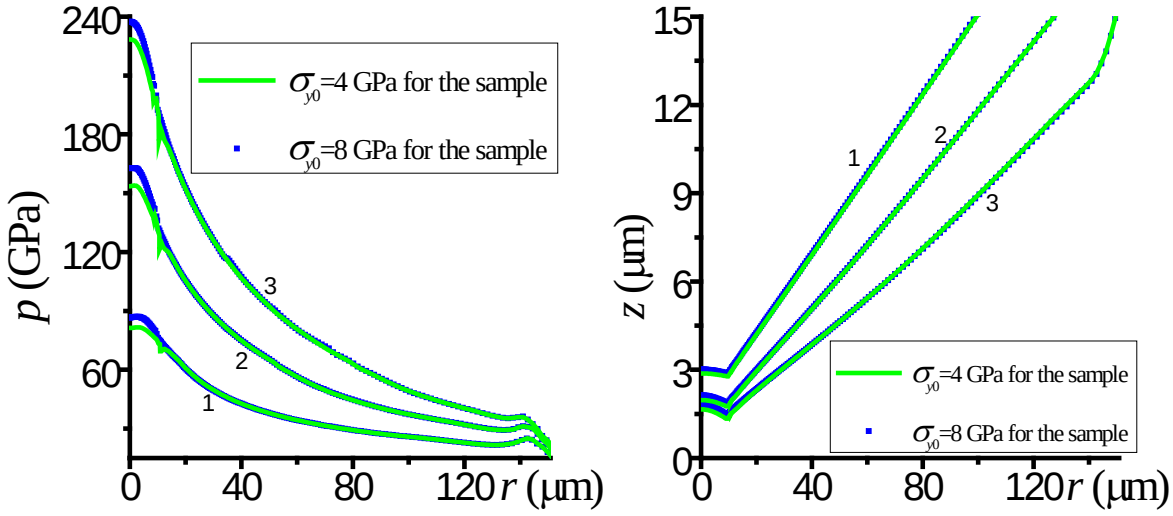

Fig. 9. Distributions of the pressure p at the contact surface of a sample (a) and z coordinate of the diamond/sample contact surface (b) for $\alpha = 9.5^{\circ}$, $r_0 = 10\,\mu\text{m}$, and the initial sample thickness $h_0 = 10\,\mu\text{m}$ under the applied normal stress σ_n: 1.05 GPa (1), 1.4 GPa (2), 1.75 GPa (3). For the green solid line: cylindrical sample of the radius $10\,\mu\text{m}$ has the same material properties as rhenium gasket (for $r > 10\,\mu\text{m}$) except for $\sigma_{y0} = 4.0$ GPa keeping $\sigma_{y0} = 8.0$ GPa for the gasket; for the blue symbol line, the entire region (gasket and sample) is rhenium. Coulomb friction is used for all contact surfaces.

Let us consider a sample material in the cylinder of the radius $10\,\mu\text{m}$ (the same as radius of the flat part, see the blue part of the zoomed area in Fig. 1c). It has the same properties as the rhenium gasket but two times smaller $\sigma_{y0} = 4.0$ GPa instead of $\sigma_{y0} = 8.0$ GPa for the gasket. Results are shown in Fig. 9. With a softer sample, the pressure gradient and consequently pressure are expected to be smaller at the center of a sample, since friction stress $\tau_f \le \tau_y$ is smaller in the equilibrium equation (14). The thickness of a softer sample is slightly smaller in Fig. 9b, which slightly increases the pressure gradient. However, the effect of a weaker friction stress dominates, which causes a lower pressure gradient and pressure in a weaker sample (Fig. 9a). However,

reduction is relatively small for such a small sample, because close to the center for any σ_{y0} friction stress reduces down to zero at the symmetry axis. Change in pressure distribution in gasket is negligible, because small changes in stresses over small sample area at fixed total force makes negligible effect on the force over the large gasket area.

Note that in experiments micro-semi balls made of nanodiamond have been placed at the center, which allowed to reach extreme pressures of 600 GPa [1] and 750 GPa [2]. This pressure increase is easily rationalized by an decrease in the sample thickness in the simplified equilibrium equation.

IV. CONCLUDING REMARKS

In this paper, FEM simulations are conducted to investigate large elastoplastic deformations of rhenium and elastic deformation of diamond under pressures up to 300 GPa in DAC, with an emphasis on the effects of geometric and material properties. Thermodynamically consistent isotropic model for large elastic and plastic deformations of a compressed material with pressure-dependent yield strength and nonlinear anisotropic model for diamond developed in [14, 24] were used.

In [14], a flat cullet was not included assuming that it should not affect results essentially. While experimental pressure distribution from [3] was reproduced without problem, the third-order elastic constants from literature [31] were modified by 20% to obtain experimentally observed cupping at the pressure of 300 GPa. Here, we found that the problem is the absence of flat cullet in simulation. With the flat cullet, we reproduced both pressure distribution and cupping in [3] using the third-order elastic constants from [27]. Also, we obtained the double cupping, both at the center and periphery, which was found in experiments [26]. In addition, significant pressure

drop in the region of cup at the periphery observed in experiments [3, 26] was reproduced as well. Thus, our model is well verified up to 300 GPa.

Transition from the material plastic flow from the center to the periphery to partial flow to the center followed by elastic deformation without or with small plasticity, all under an increasing force, is reproduced and studied. It is caused by double cupping of the diamond under extreme pressures. Paradoxical result is found that material flow to the sample center does not change the sign of the contact shear stress and pressure gradient. It is explained by finding that, due to deformation of the diamond, relative contact sliding does not change sing or is absent. Distribution of the contact shear stresses coincides with the distribution of the pressure-dependent yield strength in shear, excluding regions near the center of a sample and (for the lowest load) at the periphery. This means that plastic friction is realized by localized plastic flow below the contact surface.

We would like to stress that comparison of the effect of different parameters on the DAC mechanical behavior may strongly depend whether it is performed under the same applied load or maximum pressure at the center. For example, under the same applied load, an increase in the cullet radius reduces pressure and increases the sample thickness under the cullet, but does not affect them at the beveled surface until cupping appears. However, at the same maximum pressure at the center, the increase in the cullet radius increases pressure everywhere (except for the very center), the total force, and bending of an anvil both at the center and periphery. As mentioned, introducing cullet allows us to reproduce cupping at the periphery, which is absent at the same maximum pressure without cullet.

At the same applied force, a small increase in the bevel angle increases the pressure gradient and pressure at the center and cupping at the center, but reduces cupping at the periphery. Increase in sample thickness reduces pressure gradient and pressure at the initial compression

stages. This effect reduces with increasing compression and disappears at large compression. Small weaker sample within gasket slightly reduces pressure in a sample and does not affect gasket.

The obtained results help to understand strongly nonlinear mechanical responses of the DAC under extreme pressures and large elastoplastic deformations. In future, they may be utilized as a tool for computational optimum design of DAC. There are two main goals: (a) reach record high pressure once or multiple times and (b) reach the required high pressure in a largest possible sample once or multiple times. As the next step, we will use some of the recent experimental results up to 400 GPa in [26] for tungsten to calibrate our model and then reproduce all the experimental results in [26]. Also, phase transformations in a sample will be included, similar to how we did in [33] for boron nitride where a lower pressure range was considered.

Acknowledgements

The support of NSF (DMR-1434613), ARO (W911NF-17-1-0225), ONR (N00014-16-1-2079), and Iowa State University (Vance Coffman Faculty Chair Professorship) is gratefully acknowledged.

References

[1] L. Dubrovinsky, et al., The most incompressible metal osmium at static pressures above 750 gigapascals, Nature **525**, 226 (2015).

[2] L. Dubrovinsky, N. Dubrovinskaia, V. B. Prakapenka, and A. M. Abakumov, Implementation of micro-ball nanodiamond anvils for high-pressure studies above 6 Mbar, Nat. Commun. **3** (2012).

[3] R. J. Hemley, H. K. Mao, G. Y. Shen, J. Badro, P. Gillet, M. Hanfland, and D. Hausermann, X-ray imaging of stress and strain of diamond, iron, and tungsten at megabar pressures, Science **276**, 1242 (1997).

[4] R. Jeanloz, B. K. Godwal, and C. Meade, Static strength and equation of state of rhenium at ultra-high pressures, Nature **349**, 687 (1991).

[5] H. K. Mao and P. M. Bell, High-pressure physics: sustained static generation of 1.36 to 1.72 megabars, Science **200**, 1145 (1978).

[6] R. P. Dias, I. F. Silvera, Observation of the Wigner-Huntington transition to metallic hydrogen, Science **355**, 715–718 (2017).

[7] X.-D. Liu, P. Dalladay-Simpson, R. T. Howie, B. Li, E. Gregoryanz, Comment on "Observation of the Wigner-Huntington transition to metallic hydrogen", Science **357**, eaan2286 (2017).

[8] I. F. Silvera and R. Dias, Response to Comment on "Observation of the Wigner-Huntington transition to metallic hydrogen", Science **357**, eaan2671 (2017).

[9] B. Li, C. Ji, W. Yang, J. Wang, K. Yang, et al., Diamond anvil cell behavior up to 4 Mbar, P. Natl. Acad. Sci. USA **115**, 1713 (2018).

[10] W. C. Moss, J. O. Hallquist, R. Reichlin, K. A. Goettel, and S. Martin, Finite element analysis of the diamond anvil cell: Achieving 4.6 Mbar. Appl. Phys. Lett. **48**, 1258 (1986).

[11] W. C. Moss and K. A. Goettel, Finite element design of diamond anvils. Appl. Phys. Lett. **50**, 25 (1987).

[12] V. I. Levitas, S. B. Polotnyak, and A. V. Idesman, Large elastoplastic strains and the stressed state of a deformable gasket in high pressure equipment with diamond anvils. Strength Mater. **3**, 221 (1996).

[13] S. Merkel, R. J. Hemley, and H. K. Mao, Finite-element modeling of diamond deformation at multimegabar pressures. Appl. Phys. Lett. **74**, 656 (1999).

[14] B. Feng, V. I. Levitas, and R. J. Hemley, Large elastoplasticity under static megabar pressures: Formulation and application to compression of samples in diamond anvil cells. Int. J. Plast. **84**, 33 (2016).

[15] S. Merkel, R. J. Hemley, H. K. Mao, and D. M. Teter, Finite element modeling and ab-initio calculations of megabar stresses in the diamond anvil cell. Proceedings of the conference AIRAPT-XVII, pp 68-73 (2000).

[16] B. Feng, and V. I. Levitas, Pressure self-focusing effect and novel methods for increasing the maximum pressure in traditional and rotational diamond anvil cells. Sci. Rep. **7**, 45461, (2017)

[17] Novikov N.V., Levitas V.I., Idesman A.V. Theoretical description of thermomechanical effects in high pressure apparatus, High Press. Res. **5**, 868 (1990).

[18] V. I. Levitas and O. M. Zarechnyy, Modeling and simulation of strain-induced phase transformations under compression in a diamond anvil cell. Phys. Rev. B **82**, 174123 (2010).

[19] B. Feng, V. I. Levitas, and Y. Z. Ma, Strain-induced phase transformation under compression in a diamond anvil cell: Simulations of a sample and gasket. J. Appl. Phys. **115**, 163509 (2014).

[20] B. Feng, V. I. Levitas, and O. M. Zarechnyy, Plastic flows and phase transformations in materials under compression in diamond anvil cell: Effect of contact sliding. **114**, 043506 (2013).

[21] V. I. Levitas and O. M. Zarechnyy, Modeling and simulation of strain-induced phase transformations under compression and torsion in a rotational diamond anvil cell. Phys. Rev. B **82**, 174124 (2010).

[22] B. Feng and V. I. Levitas, Effects of gasket on coupled plastic flow and strain-induced phase transformations under high pressure and large torsion in a rotational diamond anvil cell. J. Appl. Phys. **119**, 015902 (2016).

[23] B. Feng and V. I. Levitas, Coupled phase transformations and plastic flows under torsion at high pressure in rotational diamond anvil cell: Effect of contact sliding. J. Appl. Phys. **114**, 213514 (2013).

[24] B. Feng and V. I. Levitas, Large elastoplastic deformation of a sample under compression and torsion in a rotational diamond anvil cell under megabar pressures. Int. J. Plast. **92**, 79 (2017).

[25] W. A. Bassett, Diamond anvil cell, 50th birthday, High Pressure Res **29**, 163 (2009).

[26] B. Li, C. Ji, W. Yang, ect. Diamond anvil cell behavior up to 4 Mbar. P. Natl. Acad. Sci. USA **115**, 1713 (2018).

[27] J. M. Lang and Y. M. Gupta, Experimental determination of third-order elastic constants of diamond. Phys. Rev. Lett. **106**, 125502 (2011).

[28] F. D. Murnaghan, Finite deformation of an elastic solid (Wiley, New York, 1951).

[29] V. I. Levitas, Large Deformation of Materials with Complex Rheological Properties at Normal and High Pressure (Nova Science Publishers, New York, 1996).

[30] M. H. Manghnan, K. Katahara, and E. S. Fisher, Ultrasonic equation of state of rhenium. Phys. Rev. B **9**, 1421 (1974).

[31] O. H. Nielsen, Optical phonons and elasticity of diamond at megabar stresses. Phys. Rev. B **34**, 5808 (1986).

[32] Eremets, M.I., High pressure experimental methods. (Oxford University, Oxford, 1996).

[33] B. Feng and V. I. Levitas, Coupled elastoplasticity and plastic strain-induced phase transformation under high pressure and large strains: formulation and application to BN sample compressed in a diamond anvil cell. Int. J. Plast. **96**, 156-181, (2017).